







First-principles simulation of optical emission spectra for low-pressure argon plasmas and its experimental validation

Fatima Jenina Arellano¹ , Márton Gyulai^{2,3}, Zoltán Donkó^{1,3} , Peter Hartmann³ ,
Tsanko V Tsankov⁴ , Uwe Czarnetzki⁴  and Satoshi Hamaguchi^{1,*} 

¹ Center for Atomic and Molecular Technologies, Osaka University, Osaka, Japan

² Eötvös Loránd University, Budapest, Hungary

³ Institute for Solid State Physics and Optics, Wigner Research Centre for Physics, Budapest, Hungary

⁴ Faculty of Physics and Astronomy, Experimental Physics V, Ruhr University Bochum, Bochum, Germany

E-mail: hamaguch@ppl.eng.osaka-u.ac.jp

Received 7 June 2023, revised 11 October 2023

Accepted for publication 22 November 2023

Published 18 December 2023



Abstract

Various spectral line emissions are often used for the experimental characterization of low-temperature plasmas. For a better understanding of the relation between the plasma characteristics and optical emission spectra, first-principle numerical simulations for low-pressure radio-frequency driven capacitively-coupled plasmas (CCPs) of argon have been performed by coupling one-dimensional particle-in-cell/Monte Carlo collision (PIC/MCC) simulations with a global collisional-radiative model (CRM). The only ionization and excitation mechanisms included in the PIC/MCC simulations of this study are the electron-impact ionization and excitations of the ground-state Ar atoms, as done commonly, whereas the electron-impact ionization of metastable states and other ionization mechanisms are also included in the CRM to account for the optical emission spectra. The PIC/MCC coupled CRM provides the emission spectra, which are then compared with experimental data obtained from the corresponding Ar CCPs with a gas pressure ranging from 2 Pa to 100 Pa. The comparison has shown good agreement for pressures up to about 20 Pa but increasingly notable deviations at higher pressures. The deviation is ascribed to the missing consistency between the PIC/MCC simulations and CRM at higher pressures, where the ionization from the metastable states is more dominant than that from the ground states, indicating a significant change in the electron energy distribution function due to the electron collisions with excited Ar atoms at higher pressures.

Keywords: simulations, validation, optical emission spectra OES, capacitively-coupled plasma CCP, particle-in-cell/Monte Carlo collisions PIC/MCC, collisional-radiative model CRM

1. Introduction

Low-pressure capacitively coupled plasmas (CCPs) are widely used in semiconductor and flat panel display manufacturing

for deposition and etching processes. Ions and highly reactive charge-neutral species from such plasmas are used to etch or modify material surfaces or deposit thin films. The demand to tailor the plasma-material interactions at atomic length scales [1–4] calls for higher precision in controlling the conditions of processing plasmas. This in turn requires knowledge of these conditions, which

* Author to whom any correspondence should be addressed.

can be acquired by plasma diagnostics and/or numerical simulations.

Optical emission spectroscopy (OES) is one of the most widely used diagnostics to characterize the chemical composition of plasmas and to monitor dynamic changes in the plasma conditions [5–8]. The appearance of emission lines and bands at specific wavelengths is an unmistakable marker for the presence of certain atoms or molecules in the discharge and the variation in the (relative) intensities signals changes in the plasma parameters such as the electron density, temperature and/or the dissociation degree. For a quantitative determination of these parameters, their relation to the underlying plasma conditions has to be established, which is not a simple task. In order to have a better understanding of the experimentally observed OES data, collisional-radiative models (CRMs) for plasmas with various atomic or molecular gases have been developed [9–14]. A CRM typically consists of a set of rate balance equations for the excited states of neutral and/or charged species. These equations describe the balance between population and depopulation processes and commonly include radiative transitions, as well as excitation, deexcitation, ionization, and recombination. In a global (i.e. zero-dimensional) CRM, the effects of diffusion and radiation transport are either completely neglected [15] or included only in an effective way in the form of diffusion time and escape factors [16–18].

In low-temperature plasmas, the collisional interactions are primarily due to electrons. The rates of these processes are therefore highly dependent on the electron energy distribution function (EEDF). Several studies employing a CRM to analyze experimentally-obtained OES data often assume specific EEDFs, frequently adhering to a Maxwellian shape [19–23], a distribution with an effective temperature [16, 24, 25] or two-temperature [17, 26–28] Maxwellian distributions. In other cases, general (non-Maxwellian) EEDF for CRMs are determined from Monte Carlo simulations or solved using a Boltzmann equation solver [29, 30]. Alternatively, the shape of the EEDF can be parametrized and the values of the parameters obtained from the comparison of the calculated and measured emission intensities [27].

For many discharge types, the above approaches for approximating the EEDF give satisfactory results since the shape of the electron distribution function does not vary much with the discharge conditions. In CCPs, however, the shape of the EEDF exhibits a characteristic change as a function of pressure and is commonly non-Maxwellian [31, 32]. Whenever the optical emission spectrum from such a plasma source is to be analyzed, a self-consistent approach for the modeling of the discharge, including the computation of the EEDF is essential. The most common modeling approach to achieve this goal is to use the particle-in-cell/Monte Carlo Collision (PIC/MCC) simulation technique [33–51]. This method is based on the first principles and traces charged particles (actually ‘superparticles’ that represent a high number of real particles) in the time- and space-dependent external fields and is applicable under a wide variety of conditions.

Interactions between the charged particles and the background gas, i.e. collisions, are accounted for by a stochastic (Monte Carlo) approach. The EEDF can be ‘measured’ in a PIC/MCC simulation with high spatial and temporal resolution. This information can also be used to derive the rates of any reactions of interest, like ionization or electron-impact excitation of ground-state atoms. The efficiency of PIC/MCC simulations depends on operating conditions, like the gas pressure. Their use is most advantageous at low pressures, where kinetic effects cannot be captured well by fluid models. PIC/MCC simulations have aided tremendously the investigations of CCPs, including studies of the ion energy distributions at the electrodes, charged particle dynamics, reaction rates, etc. PIC/MCC simulation codes can be validated by comparing computed discharge characteristics with experimental counterparts. Such characteristics include the plasma density, the ion flux and flux-energy distribution at the electrodes, the spatio-temporal distribution of excitation rates of atomic excited levels [22, 52–55] using various probes, ion energy analyzers, and spectroscopic methods, like phase-resolved OES [56–59]. However, to our knowledge, the combination of a PIC/MCC simulation with a CRM for calculating the emission intensities and their validation against experimental results has not been attempted yet. Such investigations have the potential to allow enhanced diagnostic tool that is able to provide complete discharge characterization by simple, non-invasive emission measurements. For this goal, it is essential that both simulation codes, PIC/MCC and CRM, run in a reasonable time.

In this study, we perform simulations to predict the optical emission spectra of low-pressure RF-driven argon (Ar) CCP by coupling a plasma simulation based on the PIC/MCC approach with a CRM, which we denote by ‘PIC+CRM’. Here, we limit the scope of our study to low-pressure ($p \leq 100$ Pa) RF-driven Ar CCPs with a symmetric pair of large parallel electrodes and use a one-dimensional (1D) PIC/MCC code to perform plasma simulation and a global CRM for Ar, which uses the electron density and the EEDF at the center of the discharge obtained from the PIC/MCC simulation to predict the optical emission spectra emitted from the central region of the plasma. Besides the experiment we also carry out experiments for measuring (i) the intensities of prominent lines in the Ar-I spectrum and (ii) the density of Ar metastable atoms in the discharge center, using tunable diode laser absorption spectroscopy (TDLAS). By comparing the results of the PIC+CRM simulations to OES measurements, we aim to verify the validity of the existing Ar CRM as well as the validity of the PIC+CRM simulation, while we also explore its limitations by comparing the measured metastable densities with those predicted by the CRM.

This paper is divided into four parts. The experimental setup of the plasma system is introduced first, followed by an explanation of the diagnostics systems. The simulation models used in this study are outlined subsequently. The experimental and simulation results are presented and discussed in section 4. The concluding remarks are given in the final section.

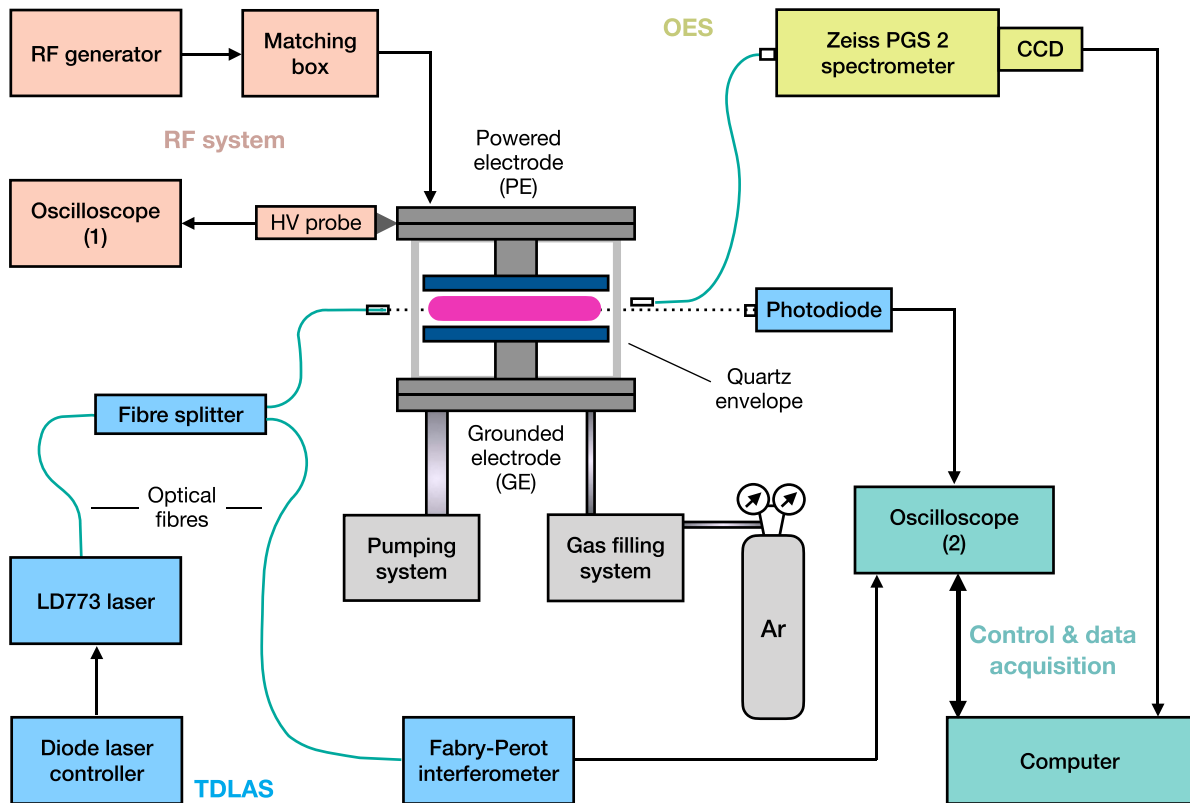


Figure 1. Schematic diagram of the experimental set-up for the TDLAS and OES measurements.

2. Experimental arrangements

2.1. Experimental setup

Figure 1 shows the scheme of the experimental setup. The experiments are conducted using a geometrically highly symmetric plane-parallel electrode CCP source (Budapest v.3 Cell) [56] such that the experimental conditions are compatible with the 1D PIC/MCC simulation. Probably the most prominent evidence for the symmetry of the experimental system is that the DC self-bias of this cell is only about 1% of the amplitude of the RF excitation voltage. The discharge cell is equipped with two symmetrical, parallel-plate stainless steel electrodes having a diameter of $2R = 14.2$ cm, which are enclosed in a quartz cylinder. The distance of the electrodes is set to $L = 4$ cm.

A turbomolecular and a rotary pump are used to evacuate the chamber down to a base pressure of 10^{-5} Pa. Ar gas is added to the system with a flow rate of 1 sccm using a mass flow controller. A needle valve on the pump side allows fine control of the gas pressure in the chamber, which is monitored by a capacitive gauge (Pfeiffer Vacuum CMR264). Our measurements cover the pressure range between $p = 2$ Pa and 100 Pa.

The upper electrode of the discharge is powered by a 13.56 MHz generator (Tokyo HY-Power RF-150) via a matching network (Tokyo HY-Power MB-300). The lower electrode is grounded. The RF voltage is monitored near the

electrode by a Solayl Vigilant RF Voltage–Current Probe. For all measurements, the peak-to-peak value of the RF voltage is fixed at $V_{pp} = 300$ V. Sufficient time is given for the electrodes to acquire their stationary temperature after any change of the gas pressure. Recent studies [59] with the same system have indicated thermalization times in the order of 30–40 min.

2.2. OES measurements

In the OES experiments, a Carl Zeiss Jena PGS-2 spectrometer equipped with an APHALAS CCD-S3600-D-UV detector is used for the measurement of the intensities of selected spectral lines belonging to the set of $2p \rightarrow 1s$ (Paschen notation) transitions in the 696–826 nm wavelength domain. The procedure involves capturing the narrow spectral segments around the emission lines of interest. In this way the line intensities are recorded without taking complete spectra of the discharge. The wavelength-dependent sensitivity of the spectrometer is determined using an RS-15 Total Flux Calibration Light Source having a certified calibration report (that specifies the radiant flux of the lamp as a function of the wavelength in the range between 300 nm and 1100 nm) provided by Gamma Scientific. This calibration procedure is based on the measurement of the intensity of the radiation emitted by this lamp (at the conditions 12 V, 8.333 A), with the same optical components (including the quartz cylinder, fiber collimator lens, and fiber optic cable) as in the plasma OES measurements.

Comparison of the measured intensity as a function of the wavelength with the certified calibration report data of the lamp allows us to derive the wavelength-dependent calibration factor that needs to be applied to the measured plasma OES recordings to eliminate the overall wavelength dependence of the sensitivity. No attempt is made to accomplish an absolute intensity calibration of the system. The OES measurements capture the light from the central, ≈ 1 cm-diameter region of the plasma, with the fiber oriented perpendicularly to the principal axis of the discharge.

Due to the relatively low intensity of some of the lines, the slit of the spectrometer is set to $100 \mu\text{m}$. The spectral resolution achieved this way still allows for the separation of the closely-situated peaks 750.4 nm and 751.5 nm , as well as 800.6 nm and 801.5 nm . However, the 772.38 nm and 772.42 nm lines are unresolved and the measured intensity values in this case represent the sum of the intensities of these two lines.

2.3. TDLAS

TDLAS is applied to obtain the gas temperature and the density of the $1s_5$ metastable Ar atoms [60–63]. The approach relies on the determination of the absorption on a selected spectral line over which the laser wavelength is scanned through. In our case, we use the transition $\text{Ar}(1s_5 \rightarrow 2p_6)$ at a wavelength of 772.376 nm .

In the experimental setup the beam of a laser diode (Toptica LD-0773-0075-DFB-1) driven by a control unit (Toptica DLC DFB PRO L) is coupled into an optical fiber, and then transferred to a splitter so that only 10% of the laser power is directed towards the plasma reactor. It passes through the middle of the plasma horizontally and is detected at the other side of the chamber by a photodiode. The remaining 90% of the power enters a Fabry–Pérot interferometer (FPI) for wavelength calibration. Both the signal transmitted through the plasma and the reference signal of the FPI are recorded by an oscilloscope (Oscilloscope (2) in figure 1), which communicates with a computer that runs a LabVIEW control and data acquisition program. To perform proper background subtraction, detector signals are recorded with and without discharge, both with laser on and off states. Assuming a dominating Doppler broadening with a Gaussian spectral profile, the amplitude of the absorption provides information about the line-integrated metastable density, while the width of the line conveys information about the gas temperature. For a more detailed description, the reader is referred to a recent publication of [64].

The Ar gas temperature T_g thus measured for the RF-driven Ar CCPs under our experimental conditions is plotted as a function of the gas pressure in figure 2. A best-fit line has been incorporated into the figure as a guide to the eye and as a measure for the scattering of the measured T_g values. The gas temperature data are used in the numerical simulations to have a better correspondence with the actual experimental conditions. The measured metastable density values obtained from TDLAS are compared with those obtained from the numerical simulations and thus will be presented later.

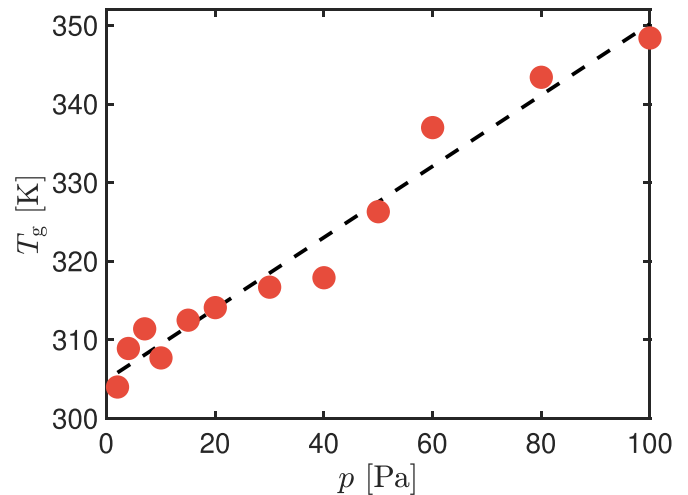


Figure 2. Gas temperature T_g of RF-driven Ar CCPs under our experimental conditions obtained from TDLAS as a function of the Ar gas pressure. The dashed curve is only a guide to the eye.

3. Simulation method

3.1. PIC/MCC simulation

The plasma simulations are based on the PIC/MCC approach. We use a spatially 1D electrostatic PIC/MCC code [50]. The simulation code has extensively been benchmarked with experimental data for several plasma characteristics [52]. Moreover, the algorithms used in the present simulation code were previously benchmarked against independent PIC/MCC implementations [65].

The code traces the electrons and Ar^+ ions present in a homogeneous background Ar gas. In our simulations, the number of superparticles inside the plasma is kept at around 10^5 per species. The spatial axis runs perpendicularly to the electrode surfaces, from the powered electrode to the grounded electrode. A numerical grid with a uniform cell size of $\Delta x = 78.1 \mu\text{m}$ is implemented [66]. The ion and electron densities and the potential as well as the electric field are defined on the points of this grid. The equations of motion are integrated through the leapfrog method with a time step of $\Delta t = 3.7 - 18.0 \text{ ps}$. In this method, particle positions and accelerations are calculated at integer time steps while velocities are calculated at half-integer time steps [39, 67, 68].

The electrodes are assumed to be plane-parallel, with a gap distance of 4 cm, corresponding to the experimental system. The simulations are executed for the same pressure range of 2–100 Pa, and RF voltage setting of 300 V (peak-to-peak) with RF driving frequency of 13.56 MHz, as in the experiments. The gas temperature values used in the calculations are taken from the TDLAS measurements, see section 2.3. The elementary processes considered in the PIC/MCC simulations are summarized in table 1. They include electron impact reactions and isotropic and backward (elastic) scattering collisions between Ar^+ and the neutral Ar atoms. The corresponding collision cross-sections were taken from the works of Hayashi [69] and Phelps [70]. As discussed above,

Table 1. List of reactions included in the PIC/MCC simulations.

Reaction	Type of reaction	Cross section/rate
$e^- + \text{Ar} \rightarrow e^- + \text{Ar}$	Elastic	[69]
$e^- + \text{Ar} \rightarrow e^- + \text{Ar}^*$	Excitations	[69]
$e^- + \text{Ar} \rightarrow 2e^- + \text{Ar}^+$	Ionization	[69]
$\text{Ar} + \text{Ar}^+ \rightarrow \text{Ar} + \text{Ar}^+$	Elastic (Isotropic)	[70]
$\text{Ar} + \text{Ar}^+ \rightarrow \text{Ar} + \text{Ar}^+$	Elastic (Backscattering)	[70]

Table 2. List of parameter settings used in PIC/MCC simulations.

Parameter	Value
Peak-to-peak voltage	300 V
Pressure	2–100 Pa
Gas temperature	304–350 K (figure 2)
Gap distance	4 cm
Time step size	3.7–18.0 ps
Numerical grid size	78.1 μm
Electron reflection coefficient	0.5
Secondary electron emission coefficient	0.07
Number of superparticles	10^5 superparticles

the only ionization and excitation mechanisms taken into account are the electron-impact ionization and excitation of the ground-state Ar atoms. Surface processes are included by implementing a constant electron reflection coefficient [71] of 0.5 and a constant Ar^+ ion-induced secondary electron emission [72] coefficient of 0.07. The data presented in this work are collected over a period of 1000 RF cycles following the convergence of the simulation. These parameter settings used in the PIC/MCC simulation are summarized in table 2.

Specific parameter constraints are implemented in the PIC/MCC simulations in order to comply with the stability and accuracy criteria: the spatial grid resolution Δx and time step Δt are set to resolve the Debye length λ_D ($\Delta x \lesssim \lambda_D$) [73] and the electron plasma frequency ω_p ($\omega_p \Delta t \leq 0.2$) [68, 74] and to comply with the Courant condition ($\nu_{\max} \Delta t \leq \Delta x$ for the vast majority of the particles, where ν_{\max} is the maximum velocity of a charged particle) [42]. Additionally, the collision probability P_j of a charged particle (such as an electron or an ion) j given by

$$P_j = 1 - \exp[-n_{\text{gs}} \sigma_T(\varepsilon) v_j^{\text{rel}} \Delta t] \quad (1)$$

is kept below 0.05 so that the chance that a particle undergoes more than one collision in one time step is marginal. In this equation, n_{gs} is the density of the background gas (target species), $\sigma_T(\varepsilon)$ is the energy-dependent total cross section of particle j , and v_j^{rel} is the velocity of particle j relative to a randomly chosen target particle. In the case of the ion-atom collisions, v_j^{rel} is determined by randomly sampling a potential collision partner from the ensemble of the thermal background gas atoms, while in the case of electron-atom collisions the target atoms are assumed to be at rest, according to the ‘cold-gas

approximation’ [50]. Depletion of the density of the ground-state gas atoms due to the presence of atoms in the excited states or due to the ionization degree is not considered in the PIC/MCC simulations. This assumption is well-justified for the conditions considered in this work since the density of the excited species is typically many orders of magnitude lower than the density of the atoms in their ground state.

The CRM requires the electron density and the EEDF from the PIC/MCC simulation. It is known (e.g. [32]) that in capacitive discharges, there are significant changes in the inter-electrode profiles of the plasma parameters with the pressure. To ensure correspondence with the experimental conditions, the data for the EEDF and the electron density are collected within a 1-cm-wide region in the center of the plasma, which reflects the volume from which the experimental emission intensities are collected. The normalization of EEDF $f_e(\varepsilon)$ is defined by [16]

$$\int_0^{\infty} f_e(\varepsilon) d\varepsilon = 1. \quad (2)$$

3.2. CRM

The numerical simulation code of the CRM developed in this study was derived from the work of Siepa *et al* [16]. The new code can take the EEDF obtained from PIC/MCC simulations as input information. The CRM calculates the population densities of the first 14 excited states of an Ar atom (1s and 2p states in Paschen’s notation) through the following balance equations:

For Ar atoms in the 1s metastable states m , namely the $1s_5$ or $1s_3$, we have

$$\begin{aligned} n_{\text{gs}} Q_{\text{gs} \rightarrow m} n_e + n_e \sum_{\substack{a=1s,2p \\ a \neq m}} n_a Q_{a \rightarrow m} + \sum_{a=2p} n_a A_{a \rightarrow m} \eta_{m \rightarrow a} \\ = \left[\left(Q_{m \rightarrow \text{gs}} + \sum_{\substack{a=1s,2p \\ a \neq m}} Q_{m \rightarrow a} + Q_{m \rightarrow \text{ion}} \right) n_e \right. \\ \left. + \sum_{a=1s} \alpha_{a,m} n_a (1 + \delta_{a,m}) + \tau_m^{-1} \right] n_m. \end{aligned} \quad (3)$$

For Ar atoms in the 1s resonant states r , namely the $1s_4$ or $1s_2$ state, we have

$$\begin{aligned} n_{\text{gs}} Q_{\text{gs} \rightarrow r} n_e + n_e \sum_{\substack{a=1s,2p \\ a \neq r}} n_a Q_{a \rightarrow r} + \sum_{a=2p} n_a A_{a \rightarrow r} \eta_{r \rightarrow a} \\ = \left[\left(Q_{r \rightarrow \text{gs}} + \sum_{\substack{a=1s,2p \\ a \neq r}} Q_{r \rightarrow a} + Q_{r \rightarrow \text{ion}} \right) n_e \right. \\ \left. + \sum_{a=1s} \alpha_{a,r} n_a (1 + \delta_{a,r}) + A_{r \rightarrow \text{gs}} \eta_{\text{gs} \rightarrow r} \right] n_r. \end{aligned} \quad (4)$$

Table 3. Constants used for collisional quenching of the $2p_n$ ($n = 1, \dots, 10$) states by the background gas [75, 76].

2p state	2p ₁₀	2p ₉	2p ₈	2p ₇	2p ₆	2p ₅	2p ₄	2p ₃	2p ₂	2p ₁
$k_{q,2p}$ ($10^{-16} \text{m}^3 \text{s}^{-1}$)	0.20	0.59	0.24	0.77	0.13	0.12	0.56	1.10	0.53	0.16

Table 4. Processes included in the CRM. Here 1s refers to one of the 1s states and 2p refers to one of the 2p states. The slash ‘/’ refers to ‘or’, e.g. ‘1s/2p’ refers to one of the 1s or 2p states.

Process name	Coefficient	Reactions	Equation	Reference
electron impact transitions from state i to state j	$Q_{i \rightarrow j}$	Ar(gs) + e \leftrightarrow Ar(1s/2p) + e Ar(1s) + e \leftrightarrow Ar(1s/2p) + e Ar(1s/2p) + e \rightarrow Ar ⁺ + 2e	Equations (6) and (7)	[77, 78] [78] [29]
spontaneous emission from higher state j to lower state i with radiation trapping	$A_{j \rightarrow i} \eta_{i \rightarrow j}$	Ar(1s ₄ /1s ₂) \leftrightarrow Ar(gs) + $h\nu$ Ar(2p) \leftrightarrow Ar(1s) + $h\nu$	Equations (8) and (9)	Table 5, [79–81]
diffusion time of metastables with $m = 1s_5$ or $1s_3$	τ_m	Ar(1s ₅ /1s ₃) + wall \rightarrow Ar(gs)	Equations (10)–(12)	[17, 21, 81, 82]
pooling ionization between two atoms in the 1s state	$\alpha_{1s,1s}$	Ar(1s) + Ar(1s) \rightarrow Ar(gs) + Ar ⁺ + e	Equations (13)–(15)	[17, 21, 81, 83, 84]
collisional quenching by Ar atoms	$k_{q,2p}$	Ar(2p) + Ar(gs) \rightarrow Ar(gs) + Ar(gs)		Table 3, [75, 76]

For Ar atoms in one of the 2p excited states, we have

$$\begin{aligned}
 & n_{\text{gs}} Q_{\text{gs} \rightarrow 2p} n_{\text{e}} + n_{\text{e}} \sum_{a=1s} n_a Q_{a \rightarrow 2p} \\
 &= \left[\left(Q_{2p \rightarrow \text{gs}} + \sum_{a=1s} Q_{2p \rightarrow a} + Q_{2p \rightarrow \text{ion}} \right) n_{\text{e}} \right. \\
 & \left. + \sum_{a=1s} A_{2p \rightarrow a} \eta_{a \rightarrow 2p} + k_{q,2p} n_{\text{gs}} \right] n_{2p}. \quad (5)
 \end{aligned}$$

Here the subscripts ‘gs’ and ‘ion’ indicate that the corresponding values are those for the ground state of Ar atom and ions, 2p denotes any of the ten 2p states considered (e.g. 2p₁₀, 2p₉, ..., 2p₁), and n_a and n_e denotes the density of excited Ar atoms at level a and that of electrons. Among the various excited states, m refers to one of the metastable states ($m = 1s_5$ or $1s_3$) and r denotes one of the resonant states ($r = 1s_4$ or $1s_2$). The collisional processes of state i with electrons that brings state i to state j are described by a rate constant $Q_{i \rightarrow j}$ while $\alpha_{1s,1s}$ denotes the collision rate for the pooling ionization of two Ar atoms in 1s state (not necessarily the same 1s state). The characteristic time for diffusion and the collisional quenching constant by the background gas are denoted by τ_m and $k_{q,2p}$, whose values are given in table 3. The Kronecker delta $\delta_{i,j}$ accounts for the pooling ionization between particles of the same type. The Einstein coefficient $A_{j \rightarrow i}$ and the escape factor $\eta_{i \rightarrow j}$ correspond to the coefficients used for the spontaneous emission from state j to state i , and radiation trapping from state i to state j processes. The reactions associated with these coefficients are listed in table 4.

The rate coefficient $Q_{i \rightarrow j}$ for an electron impact excitation from a lower state i to an upper state j is calculated using

$$Q_{i \rightarrow j} = \sqrt{\frac{2}{m_e}} \int_{\varepsilon_{ij}}^{\infty} \sigma_{ij}(\varepsilon) \varepsilon^{1/2} f_e(\varepsilon) d\varepsilon \quad (6)$$

where m_e is the electron mass, ε_{ij} is the energy difference between level i and level j , and σ_{ij} is the collision cross section [11, 25, 85, 86].

The reaction for the inverse process, $Q_{j \rightarrow i}$, is derived from the detailed balance principle and can be calculated using the equation

$$Q_{j \rightarrow i} = \frac{g_i}{g_j} \sqrt{\frac{2}{m_e}} \int_{\varepsilon_{ij}}^{\infty} \sigma_{ij}(\varepsilon) \varepsilon^{1/2} \sqrt{\frac{\varepsilon}{\varepsilon - \varepsilon_{ij}}} f_e(\varepsilon - \varepsilon_{ij}) d\varepsilon \quad (7)$$

where g_i and g_j are the statistical weights of the lower and upper states [25, 85, 86]. This expression follows from the relation between the cross sections for the forward and the reverse process, σ_{ij} and σ_{ji} i.e. $\varepsilon \sigma_{ji}(\varepsilon) = (\varepsilon + \varepsilon_{ij}) \sigma_{ij}(\varepsilon + \varepsilon_{ij})$. The cross-section data for the electron impact excitation and de-excitation processes are taken from the works of Lin (gs \rightarrow 2p) [77] and Zatsarinny and Bartschat (all other excitations) [78]. The electron impact ionization coefficient from the excited state i $Q_{i \rightarrow \text{ion}}$ is also calculated using equation (6), with the ionization cross section $\sigma_{i \rightarrow \text{ion}}$ calculated the same way as in [29].

When the integrals such as equations (6) and (7) are numerically evaluated with collision cross sections and the EEDF as integrands, we typically perform the integral up to 100 eV. At that energy, the EEDF has already decreased sufficiently under typical conditions of discharges that we are interested in for this study. The interpolation is done on the EEDF values such that the energy bins match those available in the cross-section data.

The effect of radiation trapping is expressed through the escape factor $\eta_{i \rightarrow j}$ given by [80]

$$\eta_{i \rightarrow j} = \frac{2 - \exp(-k_{ji}R/1000)}{1 + k_{ji}R}. \quad (8)$$

Here, R is the chamber radius ($R = 7.1$ cm) and k_{ji} is the absorption coefficient for the light emitted from the radiative transition from state j to state i of an Ar atom with wavelength λ_{ji} , given by

$$k_{ji} = \frac{\lambda_{ji}^3 n_i g_j A_{j \rightarrow i} m_{\text{Ar}}^{1/2}}{8\pi g_i \sqrt{2\pi k_B T_g}}, \quad (9)$$

where m_{Ar} is the mass of the Ar atom, T_g is the Ar gas temperature, and k_B is the Boltzmann constant [17, 21]. The form of the escape factor in equation (8) has been preferred over other available alternatives, e.g. [18, 87–91] since its validity appears to have been verified in other studies [81, 92].

The diffusion time τ_m for $m = 1s_5$ or $1s_3$ metastable atoms is defined by

$$\tau_m = \frac{\Lambda^2}{D_m}, \quad (10)$$

where the diffusion length Λ depends on the chamber geometry such that

$$\frac{1}{\Lambda^2} = \left(\frac{2.405}{R}\right)^2 + \left(\frac{\pi}{L}\right)^2, \quad (11)$$

and D_m is the diffusion coefficient given by

$$D_m = D_{\text{sc},m} \frac{n_{\text{sc}}}{n_{\text{gs}}} \sqrt{\frac{T_g}{T_g^0}}. \quad (12)$$

Here, $D_{\text{sc},m}$ and n_{sc} are the diffusion coefficient for the metastable atoms in state ‘ m ’ and Ar gas density at standard conditions. Following references [17, 21, 81, 82], the values of $D_{\text{sc}} n_{\text{sc}}$ for the $1s_5$ and $1s_3$ states are set to $1.8 \times 10^{18} \text{ cm}^{-1} \text{ s}^{-1}$ and $1.9 \times 10^{18} \text{ cm}^{-1} \text{ s}^{-1}$. T_g^0 is set to 300 K and the electrode gap set to $L = 4$ cm.

The rate coefficients $\alpha_{1s,1s}$ are expressed as

$$\alpha_{r,r} = 1.14 \times 10^{-20} \sqrt{\frac{16k_B T_g}{\pi m_{\text{Ar}}}} \text{ m}^3 \text{ s}^{-1} \quad (13)$$

$$\alpha_{r,m} = 2.10 \times 10^{-15} \text{ m}^3 \text{ s}^{-1} \quad (14)$$

$$\alpha_{m,m} = 1.20 \times 10^{-15} \text{ m}^3 \text{ s}^{-1}, \quad (15)$$

where α_{rr} , α_{rm} and α_{mm} are the rate coefficients for the pooling ionization between two atoms with each being in one of the resonant states, one being in one of the resonant states and the other in one of the metastable states, and each atom being in one of the metastable states, respectively [17, 21, 81, 83, 84].

The transition parameters included in the CRM are taken from the NIST database [79] and are given in table 5. The intensity of an emission line $I_{j \rightarrow i}$ (i.e. photon flux or photon

Table 5. Overview of the radiative transitions included in the CRM. The values in the table are the vacuum wavelengths of the transitions given in units of nm. The transitions marked with boldface are also examined experimentally.

$\lambda(\text{nm})$	j	i	$A_{j \rightarrow i}(\text{s}^{-1})$	g_j	g_i
104.822	1s ₂	gs	5.10×10^8	3	1
106.666	1s ₄	gs	1.19×10^8	3	1
667.728	2p ₁	1s ₄	2.36×10^5	1	3
696.543	2p ₂	1s ₅	6.39×10^8	3	5
706.722	2p ₃	1s ₅	3.80×10^6	5	5
714.704	2p ₄	1s ₅	6.25×10^5	3	5
727.294	2p ₂	1s ₄	1.83×10^6	3	3
738.398	2p ₃	1s ₄	8.47×10^6	5	5
747.117	2p ₄	1s ₄	2.20×10^4	3	3
750.387	2p ₁	1s ₂	4.45×10^7	1	3
751.465	2p ₅	1s ₄	4.02×10^7	1	3
763.511	2p ₆	1s ₅	2.45×10^7	5	5
772.376	2p ₇	1s ₅	5.18×10^6	3	5
772.421	2p ₂	1s ₃	1.17×10^7	3	1
794.818	2p ₄	1s ₃	1.86×10^7	3	1
800.616	2p ₆	1s ₄	4.90×10^6	5	3
801.479	2p ₈	1s ₅	9.28×10^6	5	5
810.369	2p ₇	1s ₄	2.50×10^7	3	3
811.531	2p ₉	1s ₅	3.31×10^7	7	5
826.452	2p ₂	1s ₂	1.53×10^7	3	3
840.821	2p ₃	1s ₂	2.23×10^7	5	3
842.465	2p ₈	1s ₄	2.15×10^7	5	3
852.144	2p ₄	1s ₂	1.39×10^7	3	3
866.794	2p ₇	1s ₃	2.43×10^6	3	1
912.297	2p ₁₀	1s ₅	1.89×10^7	3	5
922.45	2p ₆	1s ₂	5.03×10^6	5	3
935.422	2p ₇	1s ₂	1.06×10^6	3	3
965.779	2p ₁₀	1s ₄	5.43×10^6	3	3
978.45	2p ₈	1s ₂	1.47×10^6	5	3
1047.005	2p ₁₀	1s ₃	9.80×10^5	3	1
1148.811	2p ₁₀	1s ₂	1.90×10^5	3	3

counts) due to the radiative transition from state j to state i is given by

$$I_{j \rightarrow i} = n_j A_{j \rightarrow i} \eta_{i \rightarrow j}. \quad (16)$$

The calculated intensities $I_{j \rightarrow i}$ are expressed in units of photons ($\text{m}^{-3} \text{ s}^{-1}$) [93] and are proportional to the measured relative intensity. The densities of the emitting states n_j are obtained from the CRM that solves equations (3)–(5). The intensities of the lines marked in bold in table 5 are then compared with the experimental spectra.

4. Results and discussion

In this section, we first discuss some of the results of the PIC/MCC simulations, from which we evaluate the electron density and EEDF. Subsequently, a sensitivity analysis of the CRM to these input parameters is performed. The comparison of the measured and simulated intensities is later shown, along with an in-depth analysis of a possible source of discrepancy between the intensities at certain conditions.

4.1. PIC/MCC results relevant to the CRM

For better comparison with the experimental data, the information about the same spatial region of about 1 cm in the middle of the discharge is extracted from the PIC/MCC simulation. The essential input data for the CRM are the EEDF $f_e(\varepsilon)$ and electron density n_e . The electron density and a function related to the EEDF defined as

$$f_p(\varepsilon) = \varepsilon^{-1/2} f_e(\varepsilon), \quad (17)$$

are plotted in figure 3 at various pressures for discharges with a voltage amplitude of 300 V peak-to-peak. The function f_p is often called an electron energy probability function (EEDF) [94]. Also plotted in figure 3(a) are the mean energy of the bulk electrons

$$\langle \varepsilon \rangle = \int_0^{\infty} \varepsilon f_e(\varepsilon) d\varepsilon \quad (18)$$

and that of the energetic electrons above the threshold energy ε_1

$$\langle \varepsilon \rangle_{\text{ex}} = \frac{\int_{\varepsilon_1}^{\infty} \varepsilon f_e(\varepsilon) d\varepsilon}{\int_{\varepsilon_1}^{\infty} f_e(\varepsilon) d\varepsilon}. \quad (19)$$

Here we set $\varepsilon_1 = 11.55$ eV, i.e. the excitation threshold energy of the lowest excited state of Ar atoms, to represent energetic electrons that can excite ground-state Ar atoms.

It is seen in figure 3(a) that the mean energy of bulk electrons $\langle \varepsilon \rangle$ increases and that of energetic electrons $\langle \varepsilon \rangle_{\text{ex}}$ decreases rather steeply up to about 20 Pa. The decrease of $\langle \varepsilon \rangle_{\text{ex}}$ causes a corresponding decrease in excitation and ionization at higher pressures. As discussed earlier, the only ionization and excitation mechanisms used in the PIC/MCC simulation presented here are the electron-impact ionization and excitations of ground-state Ar atoms. At higher pressures, this lower ionization rate balances the decreased particle losses, and leads to lower energy per ion-electron pair created, thus allowing higher plasma density to be sustained.

It is seen in figure 3(b) that, above a certain energy, a slowly decaying energetic component is present. It reflects the ‘runaway’ secondary electrons released from the electrodes due to ion bombardment. The density of these ‘runaway’ secondary electrons in the middle of the discharge decreases with an increasing pressure due to a decrease in their mean free path. At 100 Pa, the energetic tail is completely extinguished by collisions and the electron energy does not go beyond 20 eV.

4.2. Sensitivity of calculated line intensities to input parameters of the CRM

It is also important to verify to what extent the output of the models, i.e. the spectral intensities are sensitive to a variation of the input parameters (electron density and distribution). For that, a sensitivity analysis is carried out to quantify the

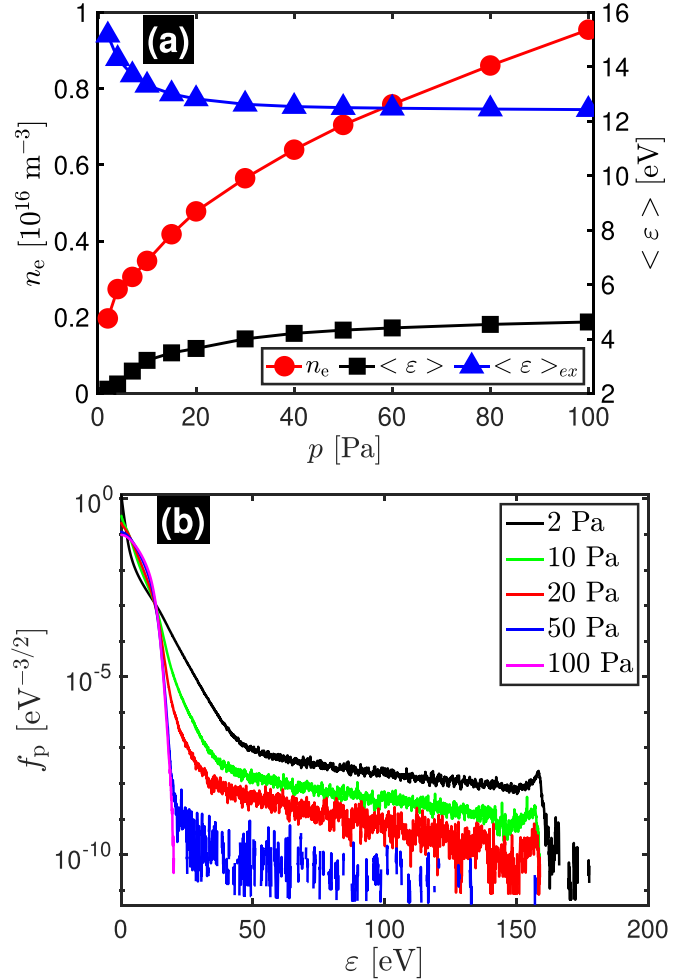


Figure 3. PIC/MCC simulation results for the central (1 cm-wide) region of 13.56 MHz RF-driven Ar CCPs with a sinusoidal voltage waveform with a peak-to-peak voltage (V_{pp} of 300 V. (a) The electron density (circles), mean electron energy for the total electron population $\langle \varepsilon \rangle$ (squares), and that for the energetic electrons above the excitation threshold voltage of 11.55 eV $\langle \varepsilon \rangle_{\text{ex}}$ (triangles), as functions of the Ar gas pressure. (b) The EEDF at different Ar gas pressures. Because $V_{\text{pp}} = 300$ eV, a sudden drop of the EEDF is seen above 150 eV (i.e. about a half of V_{pp} , corresponding to the sheath voltage) at low pressures. It should be noted that the only ionization and excitation taken into account in the simulation here are those by electron impact with ground-state Ar atoms.

effect. Figure 4(a) shows the result for the variation of the electron density used as an input parameter to the CRM at 20 Pa. Three n_e values are used for this comparison, i.e. the n_e value calculated from the PIC/MCC simulation ($n_{e,\text{PIC}} = 4.78 \times 10^{15} \text{ m}^{-3}$), its half ($0.5n_{e,\text{PIC}} = 2.39 \times 10^{15} \text{ m}^{-3}$), and its double ($2n_{e,\text{PIC}} = 9.56 \times 10^{15} \text{ m}^{-3}$). Here, the CRM used the EEDF from the same PIC/MCC simulation at 20 Pa. In the consequent discussions, the emission line denoted as 772.4 nm in figures 4(a) and (b) corresponds to the sum of the intensities of 772.38 nm and 772.42 nm lines.

The intensities are expected to increase with increasing n_e due to the increase of electron impact excitation rate to the 2p states. This becomes evident if one considers the balance for the population density of a given 2p state (equation (5)). Both

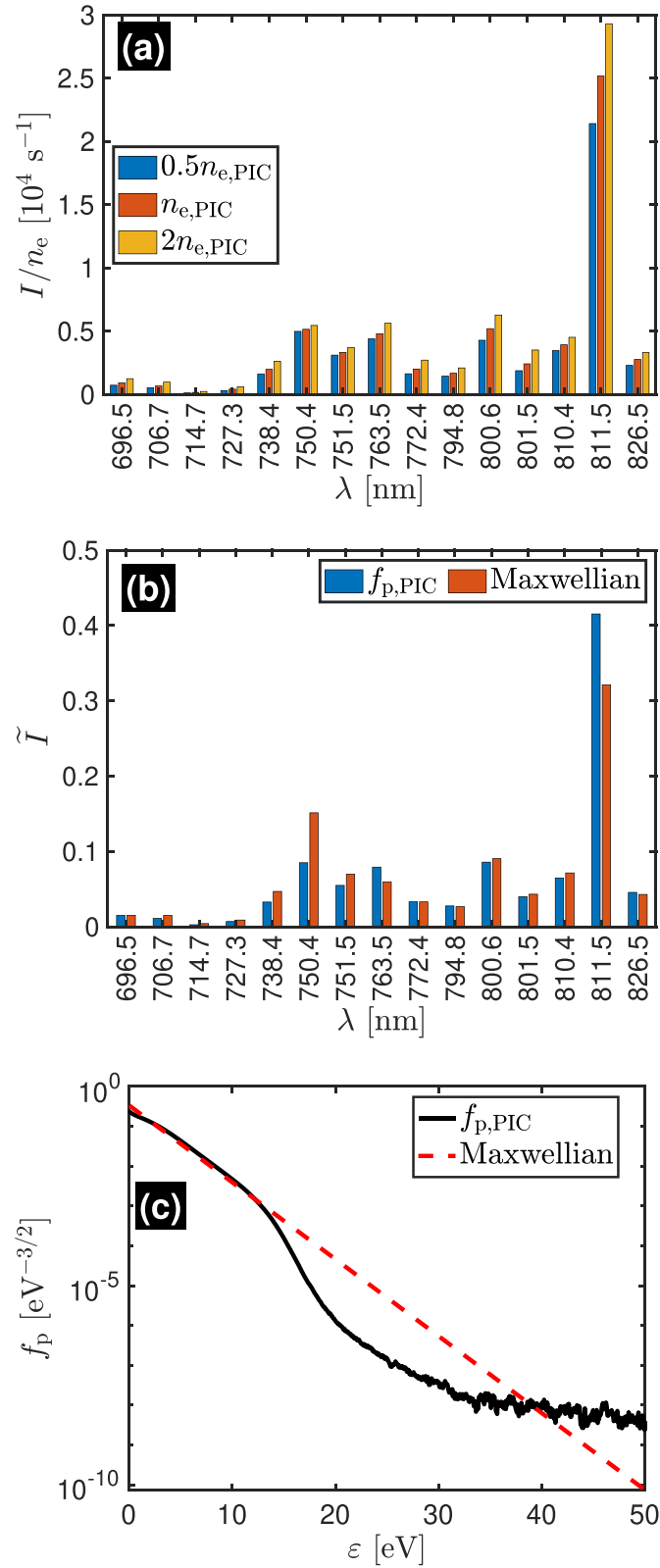


Figure 4. (a) The emission intensity I defined by equation (16) and obtained from the CRM divided by the electron density n_e with 3 different electron density values, i.e. $n_e = 0.5n_{e,\text{PIC}}$, $n_{e,\text{PIC}}$, and $2n_{e,\text{PIC}}$, where $n_{e,\text{PIC}}$ denotes the electron density obtained from the PIC/MCC simulation at 20 Pa. (b) The normalized intensity \tilde{I} , defined in equation (20), obtained from the CRM with $n_e = n_{e,\text{PIC}}$ and two different EEPFs; one from the PIC/MCC simulation at 20 Pa, denoted by $f_{p,\text{PIC}}$ and given by the solid curve in (c), and a Maxwellian distribution, given by the dotted line in (c).

the direct and the stepwise excitation processes (left-hand side of the equation) are proportional to the electron density, whereas the losses (the right-hand side) are usually dominated by the radiative transitions (the second to the last term on the right-hand side). Consequently, the emission intensity for transitions from this state varies nearly linearly with the electron density, with slight deviations due to non-linearities, introduced by the dependence of the population in the 1s block on n_e as well as the contribution of collisions to the losses of the 2p state. To amplify these more subtle nonlinear effects, the linear dependence on the plasma density is canceled out by dividing the intensity values by n_e . These ‘reduced’ values are shown in figure 4(a). For most of the lines, i.e. for most of the 2p states, only a weak dependence on the plasma density of the order of about 10% or less remains. This dependence is also almost linear, indicating that the contribution of the stepwise and cascade processes to the population of the 2p states has a linear dependence on n_e , and the collisions with electrons have a negligible contribution for the losses.

The sensitivity of the CRM to the EEPF used is also tested and shown in figure 4(b). In this figure, the resulting CRM intensities I_k (where the index k represents the individual lines for transition $j \rightarrow i$) are normalized with respect to the total intensity of the spectral lines shown, such that

$$\tilde{I} = I_k / \sum I_k. \quad (20)$$

Here ‘ $f_{p,PIC}$ ’ denotes the case when the EEPF calculated from the PIC/MCC simulation is used in the CRM, while the ‘Maxwellian’ labels the case when a Maxwellian distribution with a T_e equal to the estimated bulk T_e of the EEPF from the PIC/MCC simulation is taken as the input for the CRM. Both these EEPFs are presented in figure 4(c). The two distribution functions coincide up to around 11 eV, which is near the excitation threshold energy of the lowest excited state ($\varepsilon_1 = 11.55$ eV). Beyond 11 eV, the Maxwellian has a higher electron distribution up to around 40 eV. Since the excitation and ionization processes from the ground state occur in this energy region, a significantly higher intensity for the 750.4 nm line ($2p_1 \rightarrow 1s_2$) is observed when a Maxwellian EEPF is used. This is due to the large electron impact collision cross section of the $2p_1$ state from the ground state. This change in the shape of the spectra shows the importance of the accurate description of a non-Maxwellian EEDF for reliable intensity values.

4.3. Comparison between measured and calculated intensities

The comparison between measured and calculated intensities is presented in figure 5, for pressures of 2 Pa, 20 Pa, and 50 Pa. The data are again normalized according to equation (20), for a straightforward comparison.

The general trend of the dominant kinetic mechanisms for these pressure cases is first discussed. At low pressures, the plasma tends to be in the corona regime where the dominant processes are electron collision with the ground-state atoms and subsequent spontaneous emission from the higher excited states to the lower excited states resulting to a high intensity

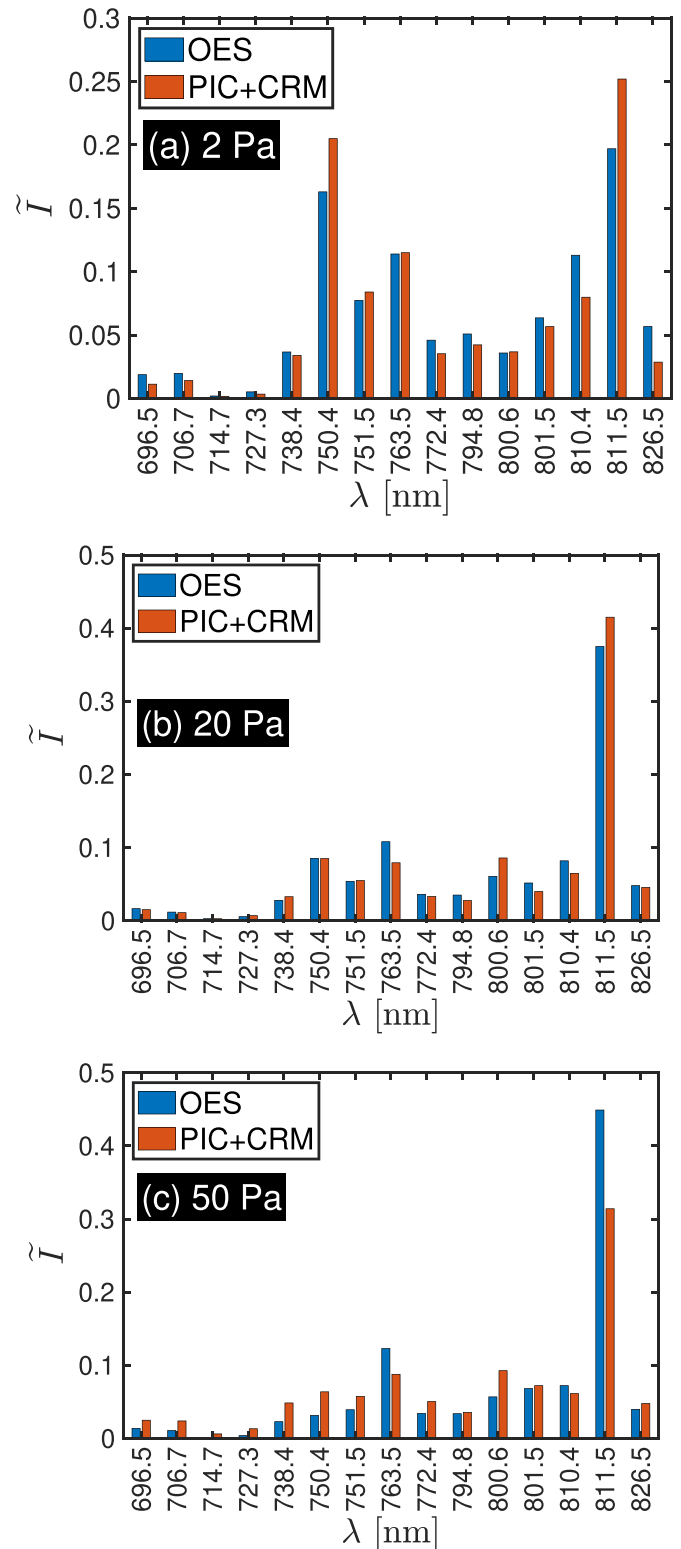


Figure 5. Measured and calculated normalized intensities at (a) 2 Pa, (b) 20 Pa, and (c) 50 Pa. As discussed earlier, the intensity line denoted as 772.4 nm corresponds to the sum of the intensities of 772.38 nm and 772.42 nm lines.

for the 750.4 nm line at 2 Pa for both measurements and simulations. Similarly, the 811.5 nm line is strong due to the high statistical weight of the $2p_9$ state, which also has a large cross section from the ground state.

The changes in the spectrum at 20 Pa with respect to the previous case of 2 Pa originate mainly from the decrease of $\langle \varepsilon \rangle_{\text{ex}}$ with the increase in pressure as shown in figure 3(a). As a result of this, a lower percentage of the excitation occurs from the ground state and stepwise excitation from the excited states becomes important. In this low-pressure non-equilibrium regime [95], the intensity of the 750.4 nm line therefore decreases relatively strongly as compared to other lines which are also populated by electron impact from excited states. The ‘metastable-dependent’ lines i.e. the ones excited by low-energy electrons from the metastable levels include 763.5 nm ($2p_6 \rightarrow 1s_5$), 800.6 nm ($2p_6 \rightarrow 1s_4$), and 811.5 nm ($2p_9 \rightarrow 1s_5$), since the $2p_6$ and the $2p_9$ states have a large collision cross section from the $1s_5$ state.

For the 50 Pa case, the 763.5 nm and 811.5 nm lines dominate the emission spectrum. The calculated intensities of these lines are significantly lower than the measured ones, while the calculated intensity of the 800.6 nm line is significantly higher than the measured line. Unlike the 800.6 nm line, the 763.5 nm and 811.5 nm lines are nonlinearly dependent on the population of the $1s_5$ state through radiation trapping since these lines also decay to the $1s_5$ state. A high $1s_5$ density (n_{1s_5}) can therefore cause a depletion of the calculated intensities by radiation trapping.

Generally, it appears that the model results tend to overestimate at higher pressures the intensities of lines for which the self-absorption is not significant, i.e. 706.7 nm, while at lower pressures they are underestimated. Simultaneously, lines with relatively high contribution of the radiation trapping, i.e. 763.5 nm, exhibit the opposite trend. This is related to an overestimation of the population of the states in the $1s$ block with the pressure increase, demonstrated and discussed later in section 4.4.1. The effect of this overestimation for the lines in the first group is higher step-wise excitation than present in the experiment, leading to higher densities of the corresponding $2p$ states. For the lines in the second group the radiation trapping effect manifests itself stronger than actually present experimentally.

These trends are also visible in figure 6 where we present the ratios of the measured (OES) and calculated (PIC+CRM) line intensities such that

$$r_k = I_{\text{OES}}(\lambda_k) / I_{\text{PIC+CRM}}(\lambda_k). \quad (21)$$

For this comparison, the line intensities have been scaled so that the average of the r_k values is 1.0. In an ideal case, i.e. in the case of a perfect agreement between the OES measurements and the PIC+CRM results, $r_k = 1$ would be recovered for each k . The data exhibit, of course, some deviations from this case, which vary as a function of the gas pressure.

In the 2 Pa case, the lines originating from the $2p_2$ state, namely the 696.5 nm, 727.3 nm, and 826.5 nm lines have higher intensities from the OES as compared to the calculated values. The common behavior of these lines suggests that the PIC+CRM may underestimate the population of the $2p_2$ state. No such conclusion can be drawn, however, for the

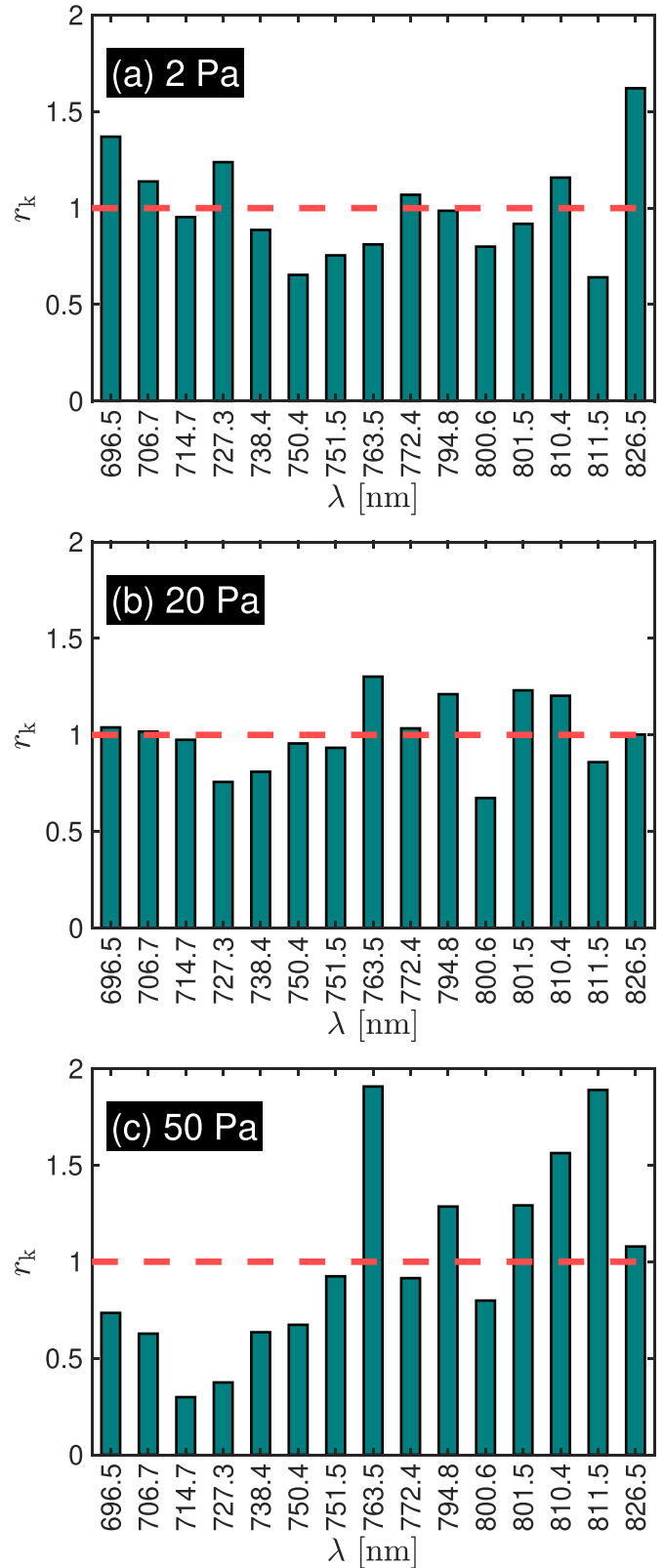


Figure 6. Normalized ratios of the intensities of the spectral lines measured using OES and calculated from PIC+CRM, at (a) 2 Pa, (b) 20 Pa, and (c) 50 Pa. As discussed earlier, the intensity line denoted as 772.4 nm corresponds to the sum of the intensities of 772.38 nm and 772.42 nm lines.

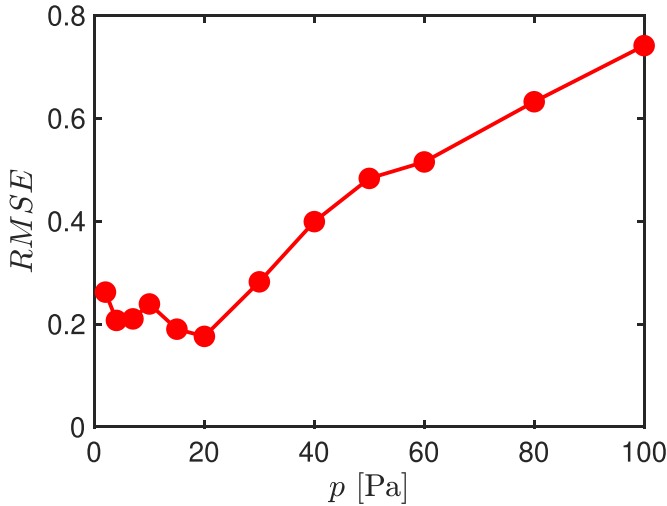


Figure 7. Root mean square error (RMSE) of the standard deviation of the OES/PIC+CRM ratio r_k to the average ratio of 1.

densities of the other states as lines originating from those do not necessarily show deviations in the same ‘direction’. The best agreement is observed for $p = 20$ Pa, where the intensity ratios deviate less than $\approx 20\%$ from the unit value. At 50 Pa, very strong deviations are observable, indicating the breakdown of the modeling approach, as will be discussed later. In this case, the 763.5 nm and 811.5 nm lines exhibit particularly strong deviations. The lower level of these lines is the $1s_5$ state, which typically has the highest concentration among the excited states. The situation at this pressure is further complicated by the fact that radiation trapping from all the $1s$ states is expected to become significant. At this pressure, excitation from all $1s$ states becomes important in the ‘medium-pressure non-equilibrium’ regime [95].

To quantify these deviations the root mean square error (RMSE) of the r_k values is calculated as

$$\text{RMSE} = \sqrt{\frac{1}{N} \sum_{k=1}^N (r_k - 1)^2}, \quad (22)$$

where $N = 15$ is the number of spectral lines. (The case of a perfect agreement between the OES and the PIC+CRM data would correspond to $\text{RMSE} = 0$). The resulting RMSE values are plotted as a function of pressure in figure 7.

For the 2 Pa case, a relatively low RMSE of 0.26 is obtained. The agreement further improves with increasing pressure, up to 20 Pa. Beyond that value, however, the RMSE starts to increase rapidly and shows the inability of the PIC+CRM approach to predict line intensities correctly. This failure of the approach at elevated pressures is suspected to be related to the presence of the excited states in the discharge, in particular the $1s_5$ state, with significant concentrations. Therefore, in the next sections we analyze the pressure dependence of the density of this state as obtained experimentally and in the CRM, and address the influence of this state on the ionization in the plasma.

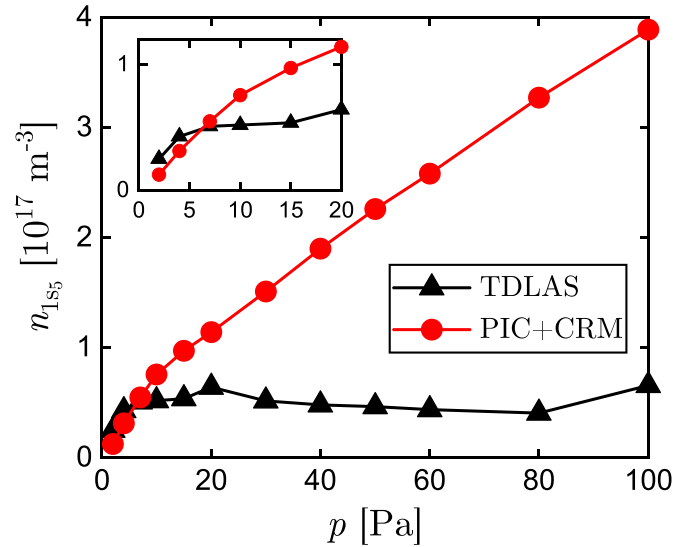


Figure 8. The densities of the $1s_5$ state Ar atoms measured with TDLAS and evaluated from the PIC+CRM simulations as functions of the gas pressure. The inset shows the same data at low pressures.

4.4. Effects of the $1s_5$ metastable state

4.4.1. Density measurement and comparison with the simulation results. The comparison of the measured and computed $1s_5$ density (n_{1s_5}) is given in figure 8 as functions of the Ar gas pressure. The laser absorption measurements show that n_{1s_5} increases with a pressure up to around 10 Pa and saturates at around $4 \times 10^{16} \text{ m}^{-3}$. Below this pressure, the measured n_{1s_5} values agree closely with the computed ones. However, above this pressure, the simulation results show a continuous increase of the n_{1s_5} . Because the electron-impact excitation to the $1s_5$ state from the ground state requires a minimum energy of 11.55 eV, figure 8 indicates that our PIC/MCC simulation either overestimates the density of the energetic electrons or underestimates the loss processes of the metastable states in our simulations.

4.4.2. Ionization from the $1s_5$ state. To further check the effect of the $1s_5$ metastable state on ionization, the contributions of the ground state and the $1s_5$ state to the ionization process were evaluated in the CRM. While the CRM described in equations (3)–(5) does not account for the ionization originating from the ground state, its rate of ionization is determined using equation (6), as is done for the excited states. Figure 9 shows a comparison of the number of ions generated per unit volume and unit time by the ionization from the ground state and the $1s_5$ metastable state calculated from the PIC+CRM simulation. This figure shows that, below 20 Pa, the ionization rate from the ground state is higher than that from the metastable state. This changes as the pressure increases and the ionization originating from the ground state decreases until it is approximately three orders of magnitude lower than that from the metastable state at 100 Pa.

Such a trend is supported by the mean energy results from figure 3(a), where the $\langle \varepsilon \rangle_{\text{ex}}$ is shown to decrease to

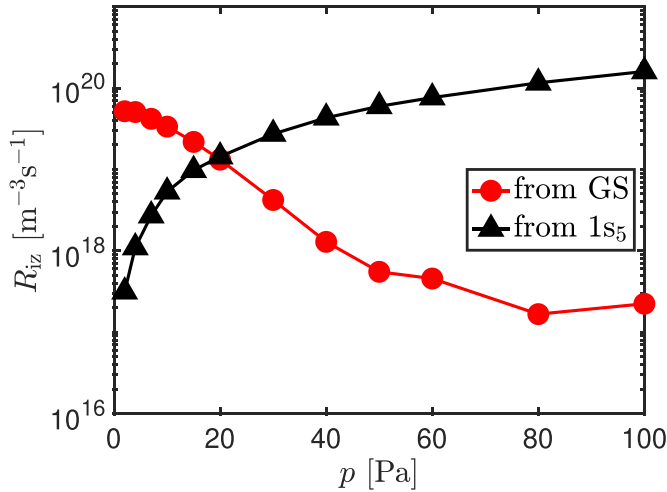


Figure 9. Rates of ionization from the ground state (denoted by ‘GS’ and filled circles) and the $1s_5$ metastable state (filled triangles). The ionization energy from the ground state is 15.8 eV and that from the $1s_5$ metastable state is 4.2 eV.

energies lower than the ground-state ionization threshold as the pressure increases. On the other hand, above 20 Pa, $\langle \varepsilon \rangle$ saturates at around 4 eV, at which ionization from the $1s_5$ metastables becomes significant as the ionization energy from the $1s_5$ metastable state is 4.2 eV. It should be noted that the simulation results presented in figure 9 used the electron density and EEDF data obtained from the PIC/MCC simulation that does not include the ionization from the $1s_5$ state. Therefore it clearly shows an inconsistency between the premise and the simulation results. Under our discharge conditions, at pressures above 20 Pa, the $1s_5$ state plays a dominant role in ionization and should not be ignored even in the PIC/MCC simulations.

4.4.3. Comparison with a Corona model. The effect of the $1s_5$ state on the excitation dynamics is investigated next. Within the framework of the corona model expected at the lower pressures, only the electron impact excitation from the ground state and the spontaneous emission from the $2p$ states (with $\eta_{i \rightarrow j} = 1$) are included. Then the balance equation for each of the $2p$ states in equation (5) simplifies to

$$n_{gs} Q_{gs \rightarrow 2p} n_e = \frac{n_{2p}}{\tau_{2p}}. \quad (23)$$

In this equation, $2p$ denotes any of the ten $2p$ states, and τ_{2p} is the lifetime of the corresponding $2p$ state defined by $1/\tau_{2p} = \sum_{i=1s} A_{2p \rightarrow i}$, where the summation is taken over all $1s$ states. Since n_e as well as n_{gs} cancel out, the ratio of intensities of two lines can be expressed as

$$\frac{I_1}{I_2} = \frac{A_1 n_{2p}}{A_2 n_{2p}} = \frac{A_1 \tau_1 Q_{gs \rightarrow 2p_i}}{A_2 \tau_2 Q_{gs \rightarrow 2p_j}}. \quad (24)$$

The subscript 1 above represents the spontaneous emission $2p_i \rightarrow 1s_x$ while 2 represents that for $2p_j \rightarrow 1s_y$. Here s_x and s_y denote some $1s$ states. The rate coefficients $Q_{gs \rightarrow 2p_i}$ and

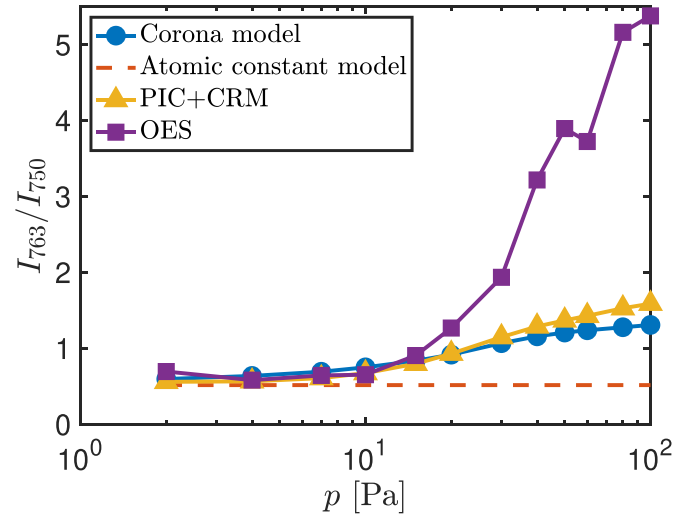


Figure 10. Intensity ratios of the 763.5 nm and 750.4 nm lines obtained from the experimental OES data (squares), calculated with the corona model (circles), PIC+CRM simulations (triangles), and the atomic constant model (dotted line).

$Q_{gs \rightarrow 2p_j}$ (i.e. $Q_{gs \rightarrow 2p_i/2p_j}$) can be expressed as in equation (6). Considering that the excitation threshold energies of the $2p$ states and their corresponding energies at the largest collision cross-section value, denoted as $\sigma_{gs \rightarrow 2p_i/2p_j, \max}$, are close to one another, the intensity can be roughly approximated in terms of the atomic constants:

$$\frac{I_1}{I_2} = \frac{A_1 \tau_1 \int_0^\infty \varepsilon^{1/2} \sigma_{gs \rightarrow 2p_i} f_e d\varepsilon}{A_2 \tau_2 \int_0^\infty \varepsilon^{1/2} \sigma_{gs \rightarrow 2p_j} f_e d\varepsilon} \simeq \frac{A_1 \tau_1 \sigma_{gs \rightarrow 2p_i, \max}}{A_2 \tau_2 \sigma_{gs \rightarrow 2p_j, \max}}. \quad (25)$$

In the last step it is further assumed that the two cross-sections have nearly identical shape and deviate only in their amplitudes (maximal values), $\sigma_{gs \rightarrow 2p_i, \max}$ and $\sigma_{gs \rightarrow 2p_j, \max}$, respectively. Equation (24) and the right-most hand side of the (25) for the 763.5 nm/750.4 nm line ratio are plotted in figure 10, referred to as a ‘corona model’ and an ‘atomic constant model.’ These data are presented along with the line ratios calculated from the PIC+CRM simulation and measured from the OES. As previously discussed in sections 4.2 and 4.3, the 763.5 nm and 750.4 nm lines strongly depend on the n_{1s_5} and n_{gs} densities, which led to the selection of this specific line ratio.

The good agreement among all cases up to around 10 Pa shows that, at these low pressures, the intensity ratio does not depend much on the plasma conditions but is rather determined by the atomic constants alone. Consequently, this ratio should not be used for diagnostic purposes of discharge at low pressures (few Pa and less). On the other hand, this provides good opportunity for checking the quality of the spectral calibration of the detector. At higher pressures, however, the line ratio becomes more sensitive to the plasma conditions. This increased sensitivity is mostly brought up by the density of the $1s_5$ state, on which the 763.5 nm line intensity is highly dependent. This shows that for a plasma with the given conditions having a pressure higher than 20 Pa, electron collisions

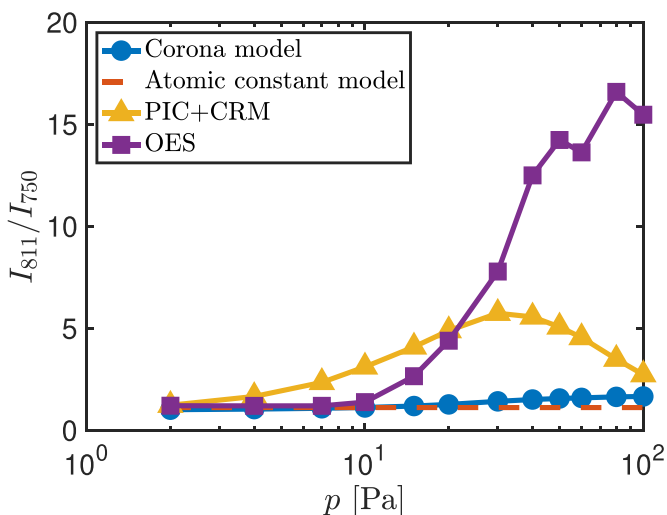


Figure 11. Intensity ratio of the 811.5 nm and 750.4 nm lines as measured from the OES, calculated using the corona model, PIC+CRM, and as estimated based on atomic data (see text).

with the metastable states already play an important role in determining optical emission and, therefore, PIC/MCC simulations is expected to yield accurate predictions for line intensity ratios only when these processes are incorporated in the numerical model self-consistently.

Although the corona model well reproduces the line ratio I_{763}/I_{750} value obtained from the PIC+CRM simulation for pressures up to 20 Pa, this good agreement between the two models does not apply to all the intensity ratios. Figure 11 shows the same set of results for another intensity ratio, namely that of the 811.5 nm and 750.4 nm lines (I_{811}/I_{750}). For this line ratio, the results show that the corona model also reproduces well the experimental ratio. However, the predictions of the full PIC+CRM model show deviations already at lower pressures. This is likely due to the behavior of the 811.5 nm line. Indeed, this is the only line from the $2p_9$ state. Further, its lower level is the $1s_5$ metastable state so that the line is subject to self-absorption. As demonstrated in figure 8, the density of the $1s_5$ state and consequently the self-absorption for this line are not correctly represented by the PIC+CRM simulation presented in this study, which causes a poor agreement between the measured and predicted (relative) intensities for the 811.5 nm line. Naturally, other lines whose lower level is the $1s_5$ state experience the same overestimation of the radiation trapping. However, all other $2p$ states have alternative radiative transitions to other $1s$ states that generally have a lower population than the $1s_5$ state. Consequently, their populations are less influenced by the overestimation of the $1s_5$ density. This suggests that the 811.5 nm line can be a sensitive indicator to assess how well the metastable density is reproduced by the model.

5. Conclusions

In this work, 1D PIC/MCC simulations were conducted for symmetrical capacitively-coupled RF Ar plasma discharges

with pressure ranging from 2 Pa to 100 Pa. The electron density and EEDF calculated from PIC/MCC simulation were used as input parameters to the CRM in order to model the Ar spectral line intensities. In the PIC/MCC simulations used in this study, the only ionization and excitation mechanisms taken into account were the electron-impact ionization and excitation of the ground-state Ar atoms. This is based on the fact that at low pressure, the metastable Ar density is typically smaller by a few orders of magnitude than the ground-state Ar density and, therefore, it is commonly assumed that the stepwise ionization from excited Ar atoms, including metastables, could be neglected in PIC/MCC simulations, which allowed a significant reduction of computation time. It should be noted that, unlike the PIC/MCC simulation used here, the CRM of this study includes the stepwise ionization from all levels of excited Ar atoms included in the model.

Comparison of the simulated intensities to the OES measurements has shown that this one-way coupling of the results from the PIC/MCC simulations into the CRM simulation (i.e. the PIC+CRM simulation) can model the spectra reasonably well up to 20 Pa. At pressures above 20 Pa, however, the calculated $1s_5$ density (n_{1s_5}) continued to increase with pressure, in contrast with the measured n_{1s_5} that was found to reach saturation. Investigation of the effect of the $1s_5$ state to the ionization and excitation dynamics of the discharge has revealed that the neglect of the loss processes of the long-lived $1s_5$ metastable state in the PIC/MCC simulation can be one of the main sources for this large n_{1s_5} discrepancy in the higher pressure range. It indicates that the EEDF and the electron density obtained from the PIC/MCC simulation of this study (without the stepwise ionization), which are used as input parameters for the CRM, are not consistent with the measured optical emission spectra in this higher pressure range. The incorporation of the Ar metastables (possibly along with a number of additional excited states) in the PIC/MCC simulation code [96–98] is therefore considered necessary to achieve a better agreement between the measured and computed optical emission spectra over a wide range of pressure.

The full integration of a CRM into the PIC/MCC simulation would require much longer computational time to simulate plasma dynamics as well as optical emission spectra. In contrast, the proposed PIC+CRM simulation can offer a practical solution for the prediction of optical emission spectra as long as the PIC/MCC simulation provides sufficiently accurate electron density and EEDF at a reasonable computational cost. The determination of the minimum number of Ar excited states that need to be included in such PIC/MCC simulations in the pressure range of our interest is deferred to a future study.

Data availability statement

The data cannot be made publicly available upon publication because no suitable repository exists for hosting data in this field of study. The data that support the findings of this study are available upon reasonable request from the authors.

Acknowledgments

F J A acknowledges the financial support of the Japan Ministry of Education, Culture, Sports, Science and Technology (MEXT) and the Japan International Cooperation Agency (JICA) Innovative Asia. T V T acknowledges the support by the DFG within the SFB1316 Project ‘Transient atmospheric plasmas: from plasmas to liquids to solids’. Z D and S H are grateful for being supported in part by the Mercator Fellowship program within the SFB1316. This research was also supported partially by the Japan Society of the Promotion of Science (JSPS) Grants-in-Aid for Scientific Research(S) 15H05736 and (A) 21H04453, JSPS Core-to-Core Program JPJSCCA2019002, Osaka University International Joint Research Promotion Programs (Type A+), Casio Science Promotion Foundation, and the Hungarian Office for Research, Development and Innovation (NKFIH) via the Grant 13446.

ORCID iDs

Fatima Jenina Arellano  <https://orcid.org/0000-0002-0543-6925>

Zoltán Donkó  <https://orcid.org/0000-0003-1369-6150>

Peter Hartmann  <https://orcid.org/0000-0003-3572-1310>

Tsanko V Tsankov  <https://orcid.org/0000-0002-7937-486X>

Uwe Czarnetzki  <https://orcid.org/0000-0002-5823-1501>

Satoshi Hamaguchi  <https://orcid.org/0000-0001-6580-8797>

References

- [1] Adamovich I et al 2017 *J. Phys. D: Appl. Phys.* **50** 323001
- [2] Adamovich I et al 2022 *J. Phys. D: Appl. Phys.* **55** 373001
- [3] Oehrlein G S and Hamaguchi S 2018 *Plasma Sources Sci. Technol.* **27** 023001
- [4] Arts K, Hamaguchi S, Ito T, Karahashi K, Knoops H, Mackus A and Kessels W M 2022 *Plasma Sources Sci. Technol.* **31** 103002
- [5] Engeln R, Klarenaar B and Guaitella O 2020 *Plasma Sources Sci. Technol.* **29** 063001
- [6] Gifford G 1990 Applications of optical emission spectroscopy in plasma manufacturing system *Advanced Techniques for Integrated Circuit Processing* vol 1392 pp 454–65
- [7] Wang S, Wendt A E, Boffard J B, Lin C C, Radovanov S and Persing H 2013 *J. Vac. Sci. Technol. A* **31** 021303
- [8] Boffard J B, Lin C C and Wendt A E 2018 *Advances In Atomic, Molecular and Optical Physics* vol 67 (Elsevier) pp 1–76
- [9] Ralchenko Y 2016 *Modern Methods in Collisional-Radiative Modeling of Plasmas* (Springer)
- [10] Van der Mullen J 1990 *Phys. Rep.* **191** 109
- [11] Tallents G 2018 *An Introduction to the Atomic and Radiation Physics of Plasmas* (Cambridge University Press)
- [12] Vlcek J 1989 *J. Phys. D: Appl. Phys.* **22** 623
- [13] Fantz U and Wunderlich D 2011 *AIP Conf. Proc.* **1344** 204–16
- [14] Akatsuka H 2019 *Adv. Phys. X* **4** 1592707
- [15] Zhu X-M and Pu Y-K 2007 *J. Phys. D: Appl. Phys.* **40** 5202
- [16] Siepa S, Danko S, Tsankov T V, Mussenbrock T and Czarnetzki U 2014 *J. Phys. D: Appl. Phys.* **47** 445201
- [17] Chai K-B and Kwon D-H 2019 *J. Quant. Spectrosc. Radiat. Transfer* **227** 136
- [18] Durocher-Jean A, Desjardins E and Stafford L 2019 *Phys. Plasmas* **26** 063516
- [19] Evdokimov K, Konischev M, Pichugin V and Sun Z 2017 *Resour. Efficient Technol.* **3** 187
- [20] Desjardins E, Laurent M, Durocher-Jean A, Laroche G, Gherardi N, Naudé N and Stafford L 2018 *Plasma Sources Sci. Technol.* **27** 015015
- [21] Iordanova S and Koleva I 2007 *Spectrochim. Acta B* **62** 344
- [22] Navrátil Z, Dvořák P, Brzobohatý O and Trunec D 2010 *J. Phys. D: Appl. Phys.* **43** 505203
- [23] Horita H, Kuwahara D, Akatsuka H and Shinohara S 2021 *AIP Adv.* **11** 075226
- [24] Boffard J B, Jung R, Lin C C and Wendt A 2010 *Plasma Sources Sci. Technol.* **19** 065001
- [25] Gangwar R, Srivastava R and Stauffer A 2013 *Eur. Phys. J. D* **67** 203
- [26] Donnelly V M 2004 *J. Phys. D: Appl. Phys.* **37** R217
- [27] Zhu X-M, Pu Y-K, Celik Y, Siepa S, Schüngel E, Luggenhölscher D and Czarnetzki U 2012 *Plasma Sources Sci. Technol.* **21** 024003
- [28] Zhu X and Pu Y 2011 *Plasma Sci. Technol.* **13** 267
- [29] Bogaerts A, Gijbels R and Vlcek J 1998 *J. Appl. Phys.* **84** 121
- [30] Pietanza L, Colonna G, De Giacomo A and Capitelli M 2010 *Spectrochim. Acta B* **65** 616
- [31] Godyak V and Piejak R 1990 *Phys. Rev. Lett.* **65** 996
- [32] Vass M, Wilczek S, Derzsi A, Horváth B, Hartmann P and Donkó Z 2022 *Plasma Sources Sci. Technol.* **31** 045017
- [33] Dawson J M 1983 *Rev. Mod. Phys.* **55** 403
- [34] Hockney R W and Eastwood J W 1988 *Computer Simulation Using Particles* (Taylor and Francis)
- [35] Birdsall C and Langdon B 1991 *Plasma Physics via Computer Simulation* (Taylor and Francis)
- [36] Birdsall C K 1991 *IEEE Trans. Plasma Sci.* **19** 65
- [37] Vahedi V, Birdsall C, Lieberman M, DiPeso G and Ronhlien T 1993 *Plasma Sources Sci. Technol.* **2** 273
- [38] Denpoh K and Nanbu K 1998 *J. Vac. Sci. Technol. A* **16** 1201
- [39] Verboncoeur J P 2005 *Plasma Phys. Control. Fusion* **47** A231
- [40] Tskhakaya D, Matyash K, Schneider R and Taccogna F 2007 *Contrib. Plasma Phys.* **47** 563
- [41] Proshina O V, Rakhimova T V, Rakhimov A T and Voloshin D G 2010 *Plasma Sources Sci. Technol.* **19** 065013
- [42] Donkó Z 2011 *Plasma Sources Sci. Technol.* **20** 024001
- [43] Lo C-W and Hamaguchi S 2011 *J. Phys. D: Appl. Phys.* **44** 375201
- [44] Becker M M, Kählert H, Sun A, Bonitz M and Loffhagen D 2017 *Plasma Sources Sci. Technol.* **26** 044001
- [45] Sun A, Becker M M and Loffhagen D 2018 *Plasma Sources Sci. Technol.* **27** 054002
- [46] Charoy T et al 2019 *Plasma Sources Sci. Technol.* **28** 105010
- [47] Lafleur T, Baalrud S and Chabert P 2016 *Phys. Plasmas* **23** 053502
- [48] Donkó Z, Derzsi A, Vass M, Schulze J, Schuengel E and Hamaguchi S 2018 *Plasma Sources Sci. Technol.* **27** 104008
- [49] Donkó Z, Hamaguchi S and Gans T 2018 *Plasma Sources Sci. Technol.* **27** 054001
- [50] Donkó Z, Derzsi A, Vass M, Horváth B, Wilczek S, Hartmann B and Hartmann P 2021 *Plasma Sources Sci. Technol.* **30** 095017
- [51] Vass M, Palla P and Hartmann P 2022 *Plasma Sources Sci. Technol.* **31** 064001
- [52] Schulenberg D A, Korolov I, Donko Z, Derzsi A and Schulze J 2021 *Plasma Sources Sci. Technol.* **30** 105003
- [53] Braginsky O, Kovalev A, Lopaev D, Proshina O, Rakhimova T, Vasilieva A, Voloshin D and Zyryanov S 2011 *J. Phys. D: Appl. Phys.* **45** 015201
- [54] Derzsi A, Lafleur T, Booth J-P, Korolov I and Donkó Z 2015 *Plasma Sources Sci. Technol.* **25** 015004
- [55] Lee S, Iza F and Lee J K 2006 *Phys. Plasmas* **13** 057102

- [56] Horváth B, Derzsi A, Schulze J, Korolov I, Hartmann P and Donkó Z 2020 *Plasma Sources Sci. Technol.* **29** 055002
- [57] Liu Y-X, Korolov I, Schüingel E, Wang Y-N, Donkó Z and Schulze J 2017 *Plasma Sources Sci. Technol.* **26** 055024
- [58] Dittmann K, Matyash K, Nemschokmichal S, Meichsner J and Schneider R 2010 *Contrib. Plasma Phys.* **50** 942
- [59] Derzsi A, Hartmann P, Vass M, Horváth B, Gyulai M, Korolov I, Schulze J and Donkó Z 2022 *Plasma Sources Sci. Technol.* **31** 085009
- [60] Makabe T 2019 *J. Phys. D: Appl. Phys.* **52** 213002
- [61] Stefanović I, Kuschel T, Schröter S and Böke M 2014 *J. Appl. Phys.* **116** 113302
- [62] Niermann B, Böke M, Sadeghi N and Winter J 2010 *Eur. Phys. J. D* **60** 489
- [63] Korolov I, Donkó Z, Hübner G, Liu Y, Mussenbrock T and Schulze J 2021 *Plasma Sources Sci. Technol.* **30** 095013
- [64] Korolov I et al 2020 *J. Phys. D: Appl. Phys.* **53** 185201
- [65] Turner M, Derzsi A, Donko Z, Eremin D, Kelly S, Lafleur T and Mussenbrock T 2013 *Phys. Plasmas* **20** 013507
- [66] Wilczek S, Schulze J, Brinkmann R, Donkó Z, Trieschmann J and Mussenbrock T 2020 *J. Appl. Phys.* **127** 181101
- [67] Birdsall C and Langdon B 2004 *Plasma Physics via Computer Simulation* (Taylor and Francis)
- [68] Alves L, Bogaerts A, Guerra V and Turner M 2018 *Plasma Sources Sci. Technol.* **27** 023002
- [69] Hayashi M 2003 Hayashi database (available at: www.lxcat.net)
- [70] Phelps A V 1994 *J. Appl. Phys.* **76** 747
- [71] Barral S, Makowski K, Peradzyński Z, Gascon N and Dudeck M 2003 *Phys. Plasmas* **10** 4137
- [72] Phelps A and Petrovic Z L 1999 *Plasma Sources Sci. Technol.* **8** R21
- [73] Mattei S, Nishida K, Onai M, Lettry J, Tran M and Hatayama A 2017 *J. Comput. Phys.* **350** 891
- [74] Horký M, Miloch W and Delong V 2017 *Phys. Rev. E* **95** 043302
- [75] Sadeghi N, Setser D, Francis A, Czarnetzki U and Döbele H 2001 *J. Chem. Phys.* **115** 3144
- [76] Chang R and Setser D 1978 *J. Chem. Phys.* **69** 3885
- [77] Chilton J, Boffard J, Schappe R and Lin C 1998 *Phys. Rev. A* **57** 267
- [78] Zatsarinny O and Bartschat K 2013 *J. Phys. B: At. Mol. Opt. Phys.* **46** 112001
- [79] Ralchenko Y 2005 *NIST Atomic Spectra Database* (available at: <https://physics.nist.gov/asd>)
- [80] Mewe R 1967 *Brit. J. Appl. Phys.* **18** 107
- [81] Siepa S L 2017 Global collisional-radiative model for optical emission spectroscopy of argon and argon-containing plasmas *Doctoral Thesis* Ruhr-Universität Bochum, Universitätsbibliothek (available at: <https://hss-opus.ub.ruhr-uni-bochum.de/opus4/frontdoor/index/index/docId/5354>)
- [82] Smirnov B 1982 Excited Atoms (Moscow Energoizdat)
- [83] Ferreira C, Loureiro J and Ricard A 1985 *J. Appl. Phys.* **57** 82
- [84] Zhiglinsky A 1994 *Handbook of constants of elementary processes with atoms, ions, electrons and photons* (Saint Petersburg)
- [85] Gangwar R, Sharma L, Srivastava R and Stauffer A 2012 *J. Appl. Phys.* **111** 053307
- [86] Yi-Qing Y, Yu X and Zhao-Yuan N 2011 *Chin. Phys. B* **20** 015207
- [87] Bhatia A and Kastner S 2000 *J. Quant. Spectrosc. Radiat. Transfer* **67** 55
- [88] Walsh P 1959 *Phys. Rev.* **116** 511
- [89] Fujimoto T 1979 *J. Quant. Spectrosc. Radiat. Transfer* **21** 439
- [90] Irons F 1979 *J. Quant. Spectrosc. Radiat. Transfer* **22** 1
- [91] Capriotti E R 1965 *Astrophys. J.* **142** 1101
- [92] Zhu X-M, Tsankov T V, Luggenhölscher D and Czarnetzki U 2015 *J. Phys. D: Appl. Phys.* **48** 085201
- [93] Fantz U 2006 *Plasma Sources Sci. Technol.* **15** S137
- [94] Godyak V, Piejak R and Alexandrovich B 1992 *Plasma Sources Sci. Technol.* **1** 36
- [95] Zhu X-M and Pu Y-K 2009 *J. Phys. D: Appl. Phys.* **43** 015204
- [96] Wen D-Q, Krek J, Gudmundsson J T, Kawamura E, Lieberman M A and Verboncoeur J P 2021 *Plasma Sources Sci. Technol.* **30** 105009
- [97] Wen D-Q, Krek J, Gudmundsson J T, Kawamura E, Lieberman M A and Verboncoeur J P 2022 *IEEE Trans. Plasma Sci.* **50** 2548
- [98] Donkó Z, Hartmann P, Korolov I, Schulenberg D A, Rohr S, Rauf S and Schulze J 2023 *Plasma Sources Sci. Technol.* **32** 065002